A full 3D plane-wave-expansion model for 1-3 piezoelectric composite structures

Mikaël Wilm, Sylvain Ballandras, Vincent Laude, and Thomas Pastureaud
Laboratoire de Physique et Métrologie des Oscillateurs/CNRS UPR 3203, associé à l'Université de Franche-Comté, 32 avenue de l'Observatoire, 25044 Besançon Cedex, France

(Received 29 November 2001; accepted for publication 31 May 2002)

The plane-wave-expansion (PWE) approach dedicated to the simulation of periodic devices has been extended to 1-3 connectivity piezoelectric composite structures. The case of simple but actual piezoelectric composite structures is addressed, taking piezoelectricity, acoustic losses, and electrical excitation conditions rigorously into account. The material distribution is represented by using a bidimensional Fourier series and the electromechanical response is simulated using a Bloch–Floquet expansion together with the Fahmy–Adler formulation of the Christoffel problem. Application of the model to 1-3 connectivity piezoelectric composites is reported and compared to previously published analyses of this problem. © *2002 Acoustical Society of America.*
[DOI: 10.1121/1.1496081]

PACS numbers: 43.38.Ar, 43.38.Fx, 43.20.Ks, 43.40.At [SLE]

I. INTRODUCTION

Piezoelectric composite transducers have been developed for medical ultrasound imaging and nondestructive evaluation to overcome the limitations of standard 1D probes. The main advantages of piezoelectric composite structures are the optimization of their electromechanical coupling factor, their low specific acoustic impedance, and their capability to be shaped on curved surfaces (for more about piezoelectric composite, see, e.g., Refs. 1–3.

Plane-wave-expansion (PWE) models[4,5] have been developed to address the description of structures exhibiting periodic in-plane or bulk nonhomogeneity. Such an approach represents an alternative to finite element computations, easy to implement and providing complementary information about the capability of any structure to guide elastic waves. Unfortunately, most of the proposed developments do not take into account piezoelectricity, acoustic losses, or simply the finite thickness of actual devices. However, the possibility to simulate, for instance, a semi-infinite substrate using a PWE approach was recently demonstrated.[6] In the present work, the PWE model for periodic structures is extended to piezoelectric composite materials. These are generally composed of a 1D (2-2 connectivity) or 2D (1-3 connectivity) array of piezoelectric elements mixed with a polymer material. Addressing the problem of periodic arrays using the proposed method allows one to compute the general properties of the device by only treating one period of the structure. The material distribution is represented using Fourier series and the electromechanical vibration using a Bloch–Floquet expansion. The Fahmy–Adler formulation of the Christoffel problem[7] has been adapted to obtain the modal distribution along the thickness of the piezoelectric composite plate.

Assessment calculations are performed for academic problems, illustrating the efficiency of the proposed approach. For instance, the identification of plate modes in a homogeneous piezoelectric material (namely the Z cut plate of quartz) has been checked. The application of the model to 2-2 and 1-3 connectivity piezoelectric composites is reported and compared to previous analyses of the same problem generally based on simpler modeling approaches or on finite element computations. The possibility to compute the harmonic admittance is emphasized, giving access to complementary data such as piezoelectric coupling, propagation losses, and vibration shapes. As a conclusion, the future extensions of the model are discussed in order to build up a comprehensive tool that is able to accurately simulate piezoelectric composite structures radiating in different media.

II. PRINCIPLES OF THE MODEL

A. Basic definitions

Figure 1 shows the general geometry of the considered structures, respectively 2-2 and 1-3 connectivity piezocomposite structures and their elementary cells. The thickness of the plate is along x_3 and wave propagation occurs along x_1 and/or x_2 depending on the addressed problem. The plate is assumed periodic along x_1 for 2D problems, and two periodicities p_1 and p_2 in the (x_1,x_2) plane are considered for 3D problems.

According to the Floquet theorem, all fields $h(\boldsymbol{r},t)$, such as displacements or stresses, propagating in such periodic structures can be expanded as infinite series

$$h(\boldsymbol{r},t)=\sum_{\boldsymbol{G}} h_{\boldsymbol{K}+\boldsymbol{G}} e^{j(\omega t-\boldsymbol{K}\cdot\boldsymbol{r}-\boldsymbol{G}\cdot\boldsymbol{r})}, \tag{1}$$

where $\boldsymbol{r}=(x_1,x_2,x_3)^T$ and $\boldsymbol{G}=(2\pi m/p_1,2\pi n/p_2,0)^T$. The upperscript ^{T} stands for transposition. $\boldsymbol{G}$ are the vectors of the reciprocal lattice and $\boldsymbol{K}$ is the wave vector. For 2D problems, K_2 and G_2 are fixed to zero. The periodicity of the structure is used to expand the material constants as Fourier series

$$\alpha(\boldsymbol{r})=\sum_{\boldsymbol{G}} \alpha_{\boldsymbol{G}} e^{-j\boldsymbol{G}\cdot\boldsymbol{r}}, \tag{2}$$

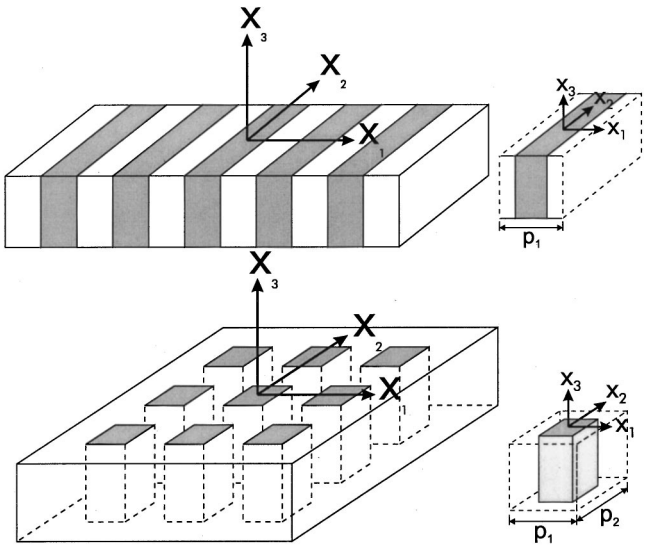

FIG. 1. General geometry of the addressed problem: respectively 2-2 and 1-3 connectivity composites and their elementary cells.

with $\alpha=\{\rho,c_{ijkl},e_{ijk},\epsilon_{ij}\}$. The terms $\alpha_{\boldsymbol{G}}$ are easily calculated, especially for different cross section shapes of 1-3 connectivity composite structures.[5]

The usual constitutive relations of piezoelectricity are then considered, together with the fundamental equation of dynamics and Poisson's condition for dielectric media:

$$T_{ij}=c_{ijkl}u_{k,l}+e_{lij}\phi_{,l}, \tag{3}$$

$$D_i=e_{ikl}u_{k,l}-\epsilon_{il}\phi_{,l}, \tag{4}$$

$$\rho\frac{\partial^2 u_j}{\partial t^2}=T_{ij,i}, \tag{5}$$

$$D_{i,i}=0. \tag{6}$$

According to Ref. 8, one can define a generalized displacement field $\boldsymbol{u}$ in which u_4 represents the electrical potential ϕ, and generalized stress vectors $\tilde{\boldsymbol{t}}_i=(T_{i1},T_{i2},T_{i3},D_i)^T$.

Inserting Eqs. (1) and (2) into Eqs. (3) and (4) yields the following expressions for the stress and electrical displacement:

$$\sum_{\boldsymbol{G}'} T_{ij\boldsymbol{K}+\boldsymbol{G}'}e^{-j\boldsymbol{G}'\cdot\boldsymbol{r}}=\sum_{\boldsymbol{G}}\sum_{\boldsymbol{G}'}[-j(K_l+G_l')\times(c_{ijkl\boldsymbol{G}}u_{k\boldsymbol{K}+\boldsymbol{G}'}+e_{lij\boldsymbol{G}}u_{4\boldsymbol{K}+\boldsymbol{G}'})e^{-j(\boldsymbol{G}+\boldsymbol{G}')\cdot\boldsymbol{r}}], \tag{7}$$

$$\sum_{\boldsymbol{G}'} D_{i\boldsymbol{K}+\boldsymbol{G}'}e^{-j\boldsymbol{G}'\cdot\boldsymbol{r}}=\sum_{\boldsymbol{G}}\sum_{\boldsymbol{G}'}[-j(K_l+G_l')(e_{ikl\boldsymbol{G}}u_{k\boldsymbol{K}+\boldsymbol{G}'}-\epsilon_{il\boldsymbol{G}}u_{4\boldsymbol{K}+\boldsymbol{G}'})e^{-j(\boldsymbol{G}+\boldsymbol{G}')\cdot\boldsymbol{r}}], \tag{8}$$

where the $'$ is introduced to differentiate summations over space harmonics relative to the dynamic fields from those relative to static distributions of material properties.

B. Matrix formulation of the problem

The orthogonality property of Fourier series components is then used to eliminate the spatial dependence of the stress and electrical displacement. The change of variable ($\boldsymbol{G}''=\boldsymbol{G}+\boldsymbol{G}'$) is first performed, then both expressions (7) and (8) are multiplied by $e^{j\boldsymbol{G}\cdot\boldsymbol{r}}$, and finally the resulting form is integrated over one period, yielding the following definition of $T_{ij\boldsymbol{K}+\boldsymbol{G}}$ and $D_{i\boldsymbol{K}+\boldsymbol{G}}$:

$$T_{ij\boldsymbol{K}+\boldsymbol{G}}=\sum_{\boldsymbol{G}'}[-j(K_l+G_l')(c_{ijkl\boldsymbol{G}-\boldsymbol{G}'}u_{k\boldsymbol{K}+\boldsymbol{G}'}+e_{lij\boldsymbol{G}-\boldsymbol{G}'}u_{4\boldsymbol{K}+\boldsymbol{G}'})], \tag{9}$$

$$D_{i\boldsymbol{K}+\boldsymbol{G}}=\sum_{\boldsymbol{G}'}[-j(K_l+G_l')(e_{ikl\boldsymbol{G}-\boldsymbol{G}'}u_{k\boldsymbol{K}+\boldsymbol{G}'}-\epsilon_{il\boldsymbol{G}-\boldsymbol{G}'}u_{4\boldsymbol{K}+\boldsymbol{G}'})]. \tag{10}$$

This operation is equivalent to an orthogonal projection of the operators on the trigonometric functional basis using the classical scalar product associated to Fourier theory (see, for instance, Ref. 9). The generalized stress vectors are then written

$$j\tilde{\boldsymbol{t}}_{i\boldsymbol{K}+\boldsymbol{G}}=\sum_{\boldsymbol{G}'}(K_l+G_l')A_{il\boldsymbol{G}-\boldsymbol{G}'}\boldsymbol{u}_{\boldsymbol{K}+\boldsymbol{G}'}\quad(i=1,2,3), \tag{11}$$

where

$$A_{il\boldsymbol{G}}(j,k)=c_{ijkl\boldsymbol{G}},\quad A_{il\boldsymbol{G}}(j,4)=e_{lij\boldsymbol{G}},\quad A_{il\boldsymbol{G}}(4,k)=e_{ikl\boldsymbol{G}},\quad A_{il\boldsymbol{G}}(4,4)=-\epsilon_{il\boldsymbol{G}}, \tag{12}$$

with $(j,k)\in[1,3]^2$.

Inserting Eqs. (1) and (2) into Eqs. (5) and (6) yields the following expressions for the propagation equation and the Poisson's condition:

$$\sum_{\boldsymbol{G}'}-j(K_i+G_i')T_{ij\boldsymbol{K}+\boldsymbol{G}'}e^{-j\boldsymbol{G}'\cdot\boldsymbol{r}}=\sum_{\boldsymbol{G}}\sum_{\boldsymbol{G}'}[\rho_{\boldsymbol{G}}(j\omega)^2u_{j\boldsymbol{K}+\boldsymbol{G}'}e^{-j(\boldsymbol{G}+\boldsymbol{G}')\cdot\boldsymbol{r}}], \tag{13}$$

$$\sum_{\boldsymbol{G}'}-j(K_i+G_i')D_{i\boldsymbol{K}+\boldsymbol{G}'}e^{-j\boldsymbol{G}'\cdot\boldsymbol{r}}=0. \tag{14}$$

Applying the same procedure to the stress and the electrical displacement provides the following expression for the generalized stress vectors:

$$(K_i+G_i)j\tilde{\boldsymbol{t}}_{i\boldsymbol{K}+\boldsymbol{G}}=\sum_{\boldsymbol{G}'}\omega^2R_{\boldsymbol{G}-\boldsymbol{G}'}\boldsymbol{u}_{\boldsymbol{K}+\boldsymbol{G}'}, \tag{15}$$

where $R_{\boldsymbol{G}-\boldsymbol{G}'}=\rho_{\boldsymbol{G}-\boldsymbol{G}'}\tilde{I}$, with

$$\tilde{I}=\begin{bmatrix}1&&&\\&1&&\\&&1&\\&&&0\end{bmatrix}.$$

In numerical computations, one has to truncate the Fourier series using a number of spatial harmonics large enough to ensure convergence. Assuming N terms in the Fourier expansions (1) and (2), the following vector notations are considered for the generalized stress and displacement fields:

$$\tilde{\boldsymbol{T}}_{i\boldsymbol{K}}=\begin{pmatrix}\tilde{\boldsymbol{t}}_{i\boldsymbol{K}+\boldsymbol{G}^1}\\ \vdots \\ \tilde{\boldsymbol{t}}_{i\boldsymbol{K}+\boldsymbol{G}^N}\end{pmatrix} \quad \text{and} \quad \tilde{\boldsymbol{U}}_{\boldsymbol{K}}=\begin{pmatrix}\boldsymbol{u}_{\boldsymbol{K}+\boldsymbol{G}^1}\\ \vdots \\ \boldsymbol{u}_{\boldsymbol{K}+\boldsymbol{G}^N}\end{pmatrix}. \tag{16}$$

The same approach is applied to matrices A_{ij} and R introduced in Eqs. (11) and (15) yielding the definitions

$$\tilde{A}_{ij}=\begin{bmatrix} A_{ij\boldsymbol{0}} & A_{ij\boldsymbol{G}^1-\boldsymbol{G}^2} & \cdots & A_{ij\boldsymbol{G}^1-\boldsymbol{G}^N} \\ A_{ij\boldsymbol{G}^2-\boldsymbol{G}^1} & A_{ij\boldsymbol{0}} & \cdots & A_{ij\boldsymbol{G}^2-\boldsymbol{G}^N} \\ \vdots & \vdots & \ddots & \vdots \\ A_{ij\boldsymbol{G}^N-\boldsymbol{G}^1} & A_{ij\boldsymbol{G}^N-\boldsymbol{G}^2} & \cdots & A_{ij\boldsymbol{0}} \end{bmatrix} \tag{17}$$

and

$$\tilde{R}=\begin{bmatrix} \rho_{\boldsymbol{0}}\tilde{I} & \rho_{\boldsymbol{G}^1-\boldsymbol{G}^2}\tilde{I} & \cdots & \rho_{\boldsymbol{G}^1-\boldsymbol{G}^N}\tilde{I} \\ \rho_{\boldsymbol{G}^2-\boldsymbol{G}^1}\tilde{I} & \rho_{\boldsymbol{0}}\tilde{I} & \cdots & \rho_{\boldsymbol{G}^2-\boldsymbol{G}_N}\tilde{I} \\ \vdots & \vdots & \ddots & \vdots \\ \rho_{\boldsymbol{G}^N-\boldsymbol{G}^1}\tilde{I} & \rho_{\boldsymbol{G}^N-\boldsymbol{G}^2}\tilde{I} & \cdots & \rho_{\boldsymbol{0}}\tilde{I} \end{bmatrix}. \tag{18}$$

Introducing the diagonal matrix Γ_i $(i=1,2,3)$ whose terms are generated by first-order spatial derivatives, Eqs. (11) and (15) can be written in the very compact form

$$j\tilde{\boldsymbol{T}}_i=\tilde{A}_{ij}\Gamma_j\tilde{\boldsymbol{U}} \quad (i=1,2,3), \tag{19}$$

$$\omega^2\tilde{R}\tilde{\boldsymbol{U}}=\Gamma_i(j\tilde{\boldsymbol{T}}_i), \tag{20}$$

with

$$\Gamma_i=\begin{bmatrix} (K_i+G_i^1)I_d & & & 0 \\ & (K_i+G_i^2)I_d & & \\ & & \ddots & \\ 0 & & & (K_i+G_i^N)I_d \end{bmatrix}. \tag{21}$$

C. Calculation of the vibration distribution along x_3

Equations (19) and (20) do not exactly yield a standard eigenvalue problem as usually defined.[7,9] However, due to the large dimension of the matrices in Eqs. (19) and (20), especially when addressing the bi-periodic problem (8 equations times N, the number of spatial harmonics in the Floquet developments along x_1 times those along x_2), one should avoid any matrix inversion. The computation time and numerical difficulties related to this operation may induce major drawbacks to the proposed method. Similarly to the procedure outlined by Peach for SAW propagation on homogeneous substrates,[10] an extended definition of eigenvalue problems is considered here, for an efficient treatment of Eqs. (19) and (20) without any matrix inversion.

The structure is assumed to be nonperiodic along the x_3 axis. As a consequence, G_3 is set to zero and K_3 depends on the other parameters of the model, namely, K_1, K_2, and ω. Writing the system of Eqs. (19) and (20), in order to identify K_3 as the eigenvalue and $(\tilde{\boldsymbol{U}}_{\boldsymbol{K}}, j\tilde{\boldsymbol{T}}_{3\boldsymbol{K}})^T$ as the eigenvector of the problem, yields after some algebra

$$\begin{bmatrix} \omega^2\tilde{R}-B & 0 \\ -C2 & I_d \end{bmatrix}\begin{pmatrix} \tilde{\boldsymbol{U}}_{\boldsymbol{K}} \\ j\tilde{\boldsymbol{T}}_{3\boldsymbol{K}} \end{pmatrix}=K_3\begin{bmatrix} C1 & I_d \\ D & 0 \end{bmatrix}\begin{pmatrix} \tilde{\boldsymbol{U}}_{\boldsymbol{K}} \\ j\tilde{\boldsymbol{T}}_{3\boldsymbol{K}} \end{pmatrix}, \tag{22}$$

with

$$\begin{aligned} &B=\sum_{i,j=1,2}\Gamma_i\tilde{A}_{ij}\Gamma_j, \quad C1=\sum_{i=1,2}\Gamma_i\tilde{A}_{i3}, \\ &C2=\sum_{j=1,2}\tilde{A}_{3j}\Gamma_j, \quad D=\tilde{A}_{33}, \end{aligned} \tag{23}$$

and where $\tilde{\boldsymbol{T}}_{3\boldsymbol{K}}$ is the generalized normal stress vector.

Solving this system yields $8N$ eigenvalues $K_3^{(r)}$ and eigenvectors, which are used to build the generalized displacement and normal stress fields. Since the eigenvectors are determined for an arbitrary constant value of the independent unknowns of the problem, one introduces the relative amplitudes $A^{(r)}$ (as for surface waves, see, e.g., Refs. 8 and 10). Using a comprehensive set of boundary conditions allows one to determine these relative amplitudes. The final form of the generalized displacement and normal stress fields is written

$$\begin{aligned} \begin{pmatrix} \boldsymbol{u}(\boldsymbol{r},t) \\ \tilde{\boldsymbol{t}}_3(\boldsymbol{r},t) \end{pmatrix} &= e^{j(\omega t-K_1x_1-K_2x_2)} \\ &\times\sum_{l=1}^{N}\left[e^{-j\boldsymbol{G}^l\cdot\boldsymbol{r}}\sum_{r=1}^{8N} A^{(r)}e^{-jK_3^{(r)}x_3}\begin{pmatrix} \boldsymbol{u}_{\boldsymbol{K}+\boldsymbol{G}^l}^{(r)} \\ \tilde{\boldsymbol{t}}_{3\boldsymbol{K}+\boldsymbol{G}^l}^{(r)} \end{pmatrix}\right]. \end{aligned} \tag{24}$$

D. Boundary conditions

Note that the case of bulk waves propagating along the (x_1,x_2) plane in an infinite medium along x_3 can be easily computed using Eq. (22), simply by setting $K_3=0$ and by solving the resulting problem $\omega^2\tilde{R}\tilde{\boldsymbol{U}}=B\tilde{\boldsymbol{U}}$, where ω is computed for each (K_1,K_2) defined in the first Brillouin zone $[0,2\pi/p_{1/2}]$ ($p_{1/2}$ being the periods of the structure).

However, a large variety of boundary conditions can be applied to simulate actual operating conditions of a piezoelectric composite structure. The mechanical boundary conditions require the nullity of stress components normal to surfaces (stress free definite boundaries in air or in a vacuum) or the physical validity of the partial modes that have to be included in the normal mode expansion (24) (semi-infinite medium). In this latter case, one has to select the values of K_3 with respect to this condition. Using a criterion based on the sign of the mean Poynting vector[1,10] of each partial mode (in the case of propagative modes) or on the sign of the imaginary part of each $K_3^{(r)}$ (in the case of evanescent modes), an unambiguous modal selection can be performed. For plate devices, both sides are assumed stress free. Other kinds of mechanical boundary conditions may be applied (for instance, radiation conditions, see Ref. 11), but they have not been implemented yet. The stress free condition is then written independently from the space coordinates

x_1 and x_2, as previously explained for the propagation equation and Poisson's equation, yielding the following expressions:

$$\sum_{r=1}^{8N} A^{(r)} T_{3j\mathbf{K}+\mathbf{G}^i}^{(r)} e^{-jK_3^{(r)}h} = 0 \quad (i=1,...,N) \quad (j=1,2,3), \tag{25}$$

where $x_3 = h$ at the surface.

From the electrical point of view, in the case of a definite boundary, two kinds of boundary conditions have been considered. The first one is the continuity of the potential and of the normal component of the electrical displacement at the surface. In the air, one can write

$$\Delta \phi^{\text{air}} = 0, \tag{26}$$

$$D_3^{\text{air}} = -\epsilon_0 \frac{\partial \phi^{\text{air}}}{\partial x_3}, \tag{27}$$

where Δ is the Laplacian. The continuity conditions at the surface yield

$$\phi^{\text{substrate}}|_{x_3=h} = \phi^{\text{air}}|_{x_3=h}, \tag{28}$$

$$D_3^{\text{substrate}}|_{x_3=h} - D_3^{\text{air}}|_{x_3=h} = 0. \tag{29}$$

The boundary condition expressions are finally obtained after some algebra as

$$\sum_{r=1}^{8N} A^{(r)} [D_{3\mathbf{K}+\mathbf{G}^i}^{(r)} - \epsilon_0 |\kappa| \phi_{\mathbf{K}+\mathbf{G}^i}^{(r)}] e^{-jK_3^{(r)}h} = 0 \quad (i=1,...,N), \tag{30}$$

with $|\kappa| = \sqrt{(K_1+G_1)^2 + (K_2+G_2)^2}$.

The second boundary condition considered is setting the surface potential homogeneously to a given value V_0, for instance 0 V for a shorted surface or 1 V for an active electrode. Considering one period and infinitely close electrodes, the potential is written

$$\phi(\mathbf{r},t)|_{x_3=h} = V_0 e^{j\omega t}, \tag{31}$$

yielding

$$\sum_{i=1}^{N} \left[e^{-j\mathbf{G}^i \cdot \mathbf{r}} \sum_{r=1}^{8N} A^{(r)} \phi_{\mathbf{K}+\mathbf{G}^i}^{(r)} e^{-jK_3^{(r)}h} \right] = V_0 e^{j(K_1 x_1 + K_2 x_2)}. \tag{32}$$

Applying the orthogonal projection, one finally obtains the desired boundary conditions

$$\sum_{r=1}^{8N} A^{(r)} \phi_{\mathbf{K}+\mathbf{G}^i}^{(r)} e^{-jK_3^{(r)}h} = V_0 \left(\text{sinc}\left((K_1+G_1^i)\frac{p_1}{2} \right) \right) \left(\text{sinc}\left((K_2+G_2^i)\frac{p_2}{2} \right) \right) \quad (i=1,...,N). \tag{33}$$

In the case of homogeneous boundary conditions, one has to set up a boundary condition system exhibiting $8N$ equations (the number of independent unknowns). The modes of the structure correspond to the zeros of the determinant of this system, for which nontrivial solutions can then be obtained. For each of these modes, it is possible to compute the relative amplitude $A^{(r)}$ by setting one of them equal to an arbitrary value and then deducing the others by solving the boundary condition system. Thus the actual nature of the corresponding vibration can be identified.

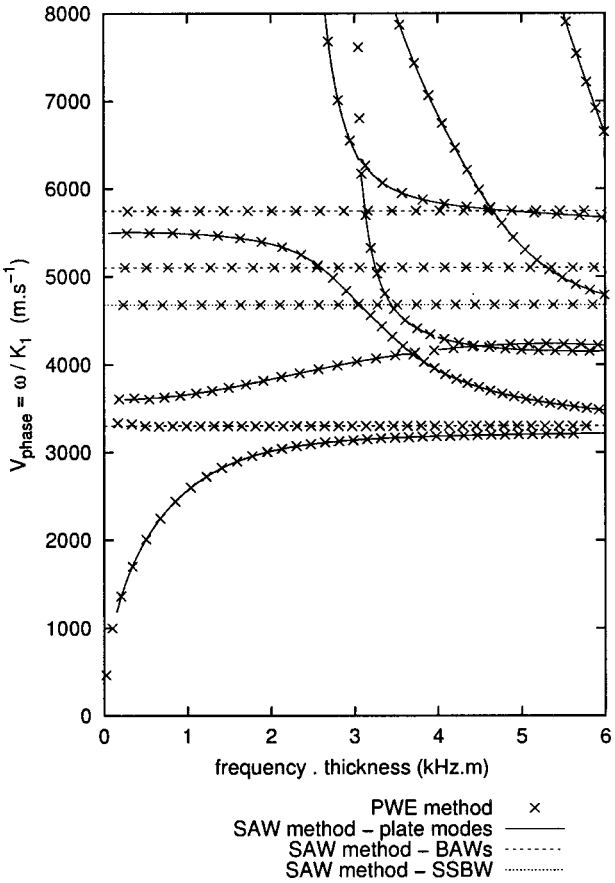

FIG. 2. Comparison between standard Green's function computation (solid and dashed lines) and the proposed approach (cross markers) to identify the acoustic modes of a (ZX) quartz plate. The plate modes (Lamb waves) are found, such as the three BAWs (bulk acoustic waves) and the SSBW (surface skimming bulk wave). The BAWS are the longitudinal, fast shear and slow shear ones at, respectively, 5748, 5103.3, and 3300.5 m s^{-1}. The SSBW celerity is 4678 m s^{-1}. Contrary to the BAWs, its wave vector is not parallel to the surface while its Poynting vector is such. The two isolated points on the top of the figure are in fact in the continuity of a Lamb mode. Indeed, the SAW dedicated method computation is not complete for the corresponding mode because of the difficulty to follow modes which cross each other.

E. Harmonic admittance

Using the above-mentioned electrical boundary conditions allows one to simulate the excitation conditions of piezoelectric composite materials and to derive the harmonic admittance for a single cell by computing the charge distribution on the active electrode. In this approach, one has to consider K_1 and K_2 as excitation parameters governing the excitation potential distribution as follows,

$$V_{mn} = V_0 e^{-jK_1 m p_1} e^{-jK_2 n p_2}, \tag{34}$$

where p_1 and p_2 are, respectively, the periodicity along x_1 and x_2 as previously defined (see Fig. 1). For instance, an alternation of the sign of the potential excitation along x_1 is

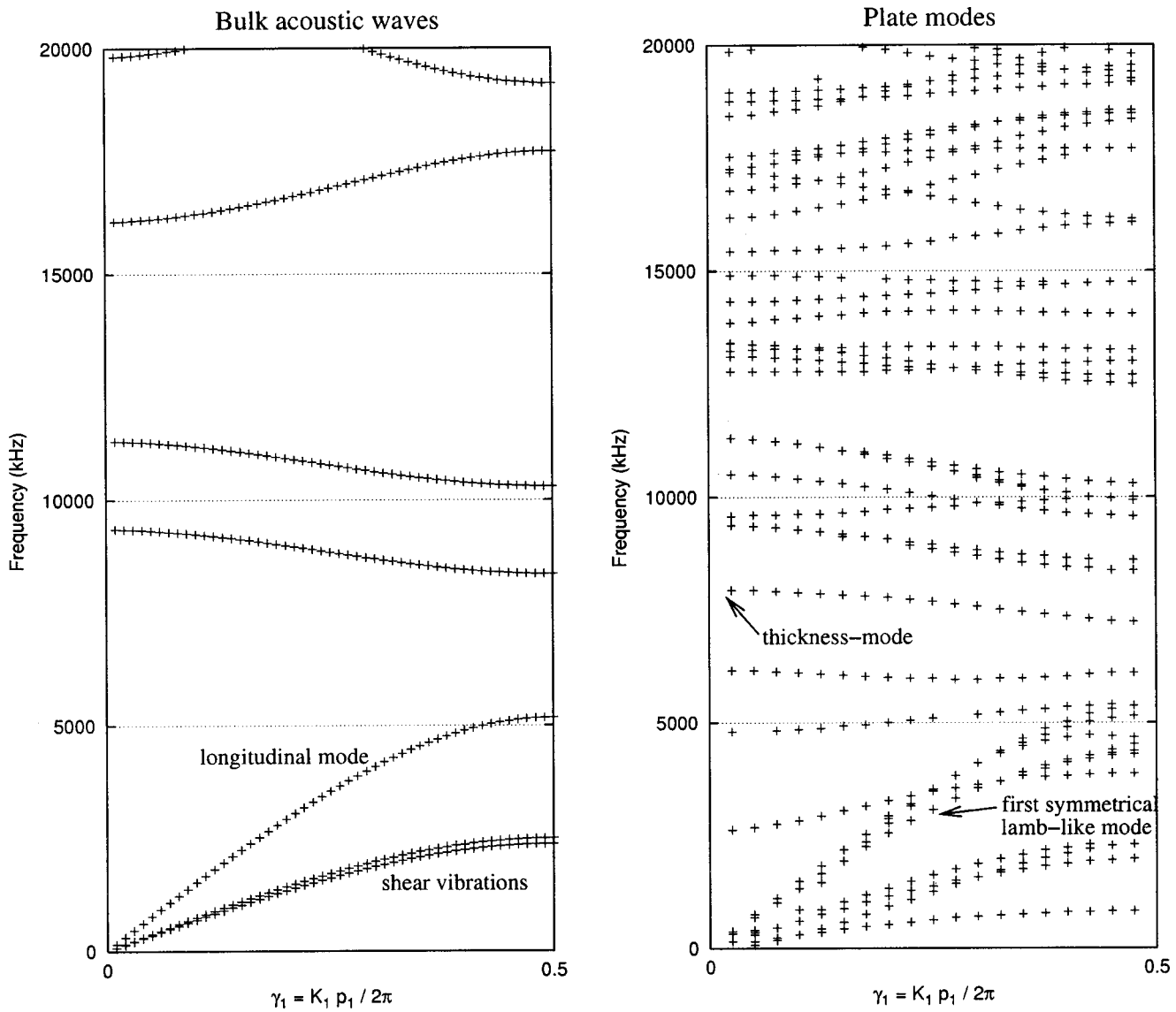

FIG. 3. Dispersion curves of the 2-2 connectivity composite of Fig. 1. Left: bulk acoustic waves propagating in the (x_1,x_2) plane. Right: plate modes of the finite-thickness composite given by the minima of the boundary condition system determinant. Bulk modes are found too with this second computation, so that bulk and plate modes are discriminated comparing the two figures.

obtained by setting $K_1=\pi/p_1$. For more details about the harmonic admittance, see Ref. 12. The charge distribution at the active interface is directly given by the difference between the normal electrical displacement in the material and in a vacuum (assuming ideally thin electrodes). Integrating this distribution along one period and multiplying the result by the angular frequency provides the harmonic admittance written $(i=1,...,N)$

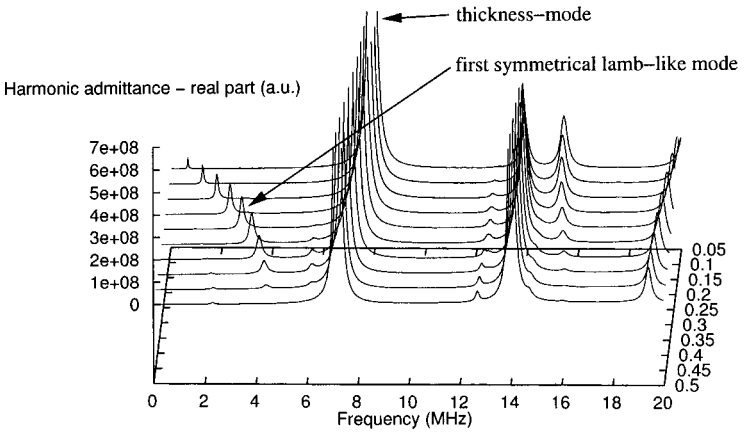

FIG. 4. Real part of the harmonic admittance (conductance) of the 2-2 connectivity piezoelectric composite material of Fig. 1. Resonance frequencies are given by the maxima of the conductance. The admittance is truncated since the thickness mode has a great amplitude compared to the other modes. We can derive from this calculus and the previous curves of Fig. 3 dispersion curves for piezoelectrically coupled plate modes, since conductance maxima indicate vibrating modes in the same manner as dispersion curves.

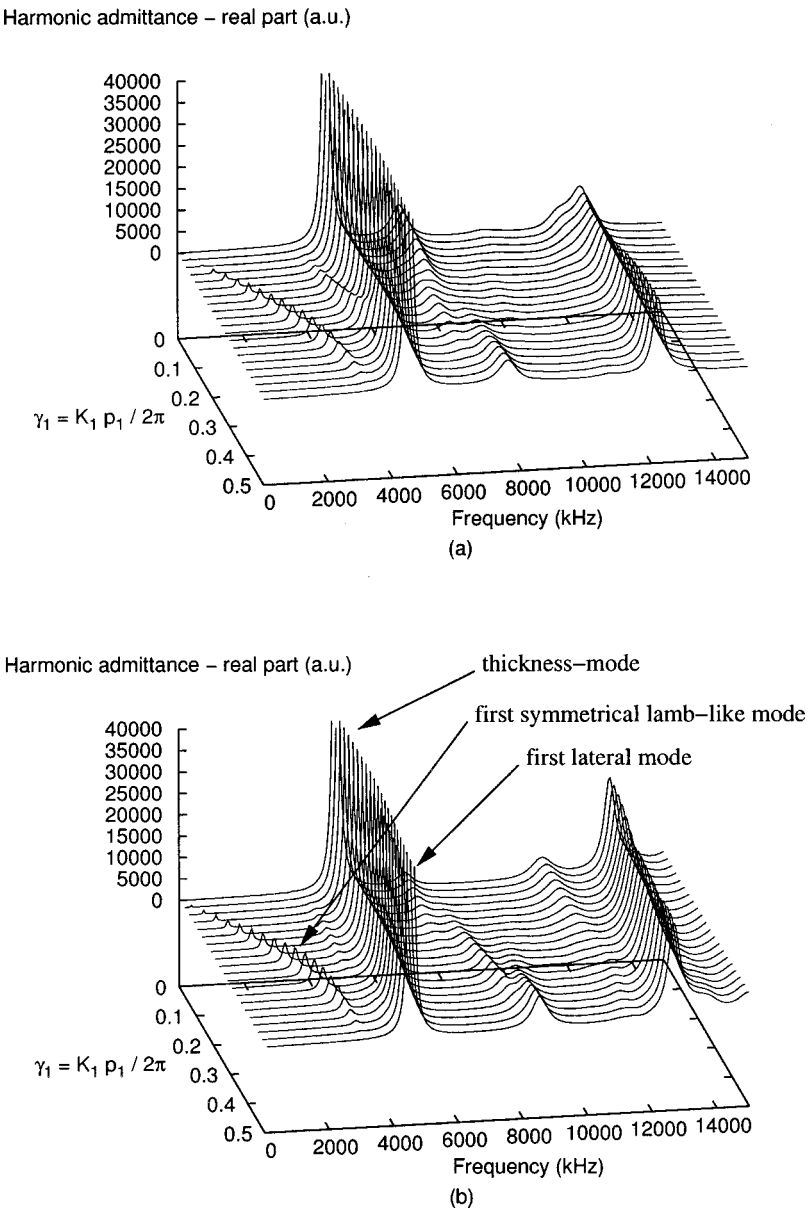

FIG. 5. Comparison between finite element (a) and PWE (b) calculations of the harmonic admittance of the 1-3 piezoelectric composite of Fig. 1. The first symmetrical Lamb-like wave, the thickness mode, and the well-known first lateral mode are indicated in the PWE curves. The displacement fields of these modes are respectively shown in Figs. 6–8.

$$Y(K_1,K_2,\omega) = j\omega \sum_{i=1}^{N} \left[\sum_{r=1}^{8N} A^{(r)} (D_{3\mathbf{K}+\mathbf{G}^i}^{(r)} - \epsilon_0 |\kappa| \phi_{\mathbf{K}+\mathbf{G}^i}^{(r)}) e^{-jK_3^{(r)}h} \right] \times \left(p_1 \mathrm{sinc}\left((K_1 + G_1^i)\frac{p_1}{2} \right) \right) \left(p_2 \mathrm{sinc}(K_2 + G_2^i)\frac{p_2}{2} \right). \quad (35)$$

This harmonic admittance provides precious information about the way the modes are piezoelectrically coupled, but also concerning frequency band-gap phenomena arising in periodic structures. It is also very useful to derive mutual admittances[12] allowing us then to evaluate cross-coupling effects for a given geometry of transducers. This latter point will be addressed in future works.

Note that in all the presented theoretical developments, the material constants are assumed complex, so that elastic, piezoelectric, and dielectric losses can be taken into account.[13]

III. NUMERICAL APPLICATION OF THE MODEL

A. Acoustic plate modes in quartz

This first example was chosen simply to validate the approach. The problem is the calculation of acoustic plate modes of a Z cut plate of quartz, with propagation along the *X* axis. By considering only the fundamental term in the Fourier and Floquet series, one can directly simulate the acoustic propagation in a homogeneous material of finite thickness. The results are easily compared to those of SAW (surface acoustic wave) dedicated simulation tools developed in our group.[14] This comparison is shown in Fig. 2 where the phase velocity is displayed as a function of the frequency-thickness product. A very good agreement between both calculations for piezoelectrically coupled modes can be observed. The proposed approach also allows one to identify the noncoupled modes of the plate, and also modes which energy propagates parallel to the plate surfaces (Poynting vector parallel to the surfaces), but are not affected by the plate thickness and hence are not dispersive. Four modes of

this kind are found in Fig. 2, and are the slow shear, fast shear, and longitudinal bulk acoustic waves, plus a fast shear SSBW (surface skimming bulk wave, see Ref. 1).

B. 2-2 connectivity piezoelectric composite

The geometry of the considered structure is shown in Fig. 1. The thickness of the plate was set to 200 μm; the period along x_1 was 150 μm with a 100-μm width PZT ridge.

In that case, different computations were performed to identify the modes propagating in the structure. Bulk modes were first determined assuming an infinite thickness for the plate and $K_3=0$. The eigenmodes of the finite thickness plate were then extracted assuming that both surfaces are electrically shorted. Finally, the harmonic admittance was computed to discriminate piezoelectrically coupled modes. The top surface is submitted to a harmonic excitation, whereas the back surface is grounded. All computations were performed considering six spatial harmonics. It should be emphasized that using more spatial harmonics yields a more nearly accurate prediction of the frequency location of the modes. Considering six harmonics represents a trade-off between accuracy and computation time. The results obtained for the three different computations are reported in Figs. 3 and 4. Figure 3 shows the bulk eigenmodes propagating in the (x_1,x_2) plane and the plate eigenmodes of the finite-thickness configuration, and Fig. 4 displays the real part of the harmonic admittance of the piezoelectric composite for all couples $(\omega,\gamma_1=K_1p_1/2\pi)$. In the case of infinite thickness of the plate, one can easily identify the first three modes as in-plane and thickness shear vibrations, and in-plane longitudinal propagation. The latter strongly contributes to the first symmetrical Lamb wave. In the case of the finite thickness configuration, many couples (ω,γ_1) are found to minimize the determinant of the boundary condition system. However, some of these values correspond to local minima of this determinant and not to physical solutions of the problem. For instance, bulk modes appear for the finite-thickness configuration, too, and can be discriminated using the results of the case of infinite thickness. In Fig. 4, it can be seen that the piezoelectrically coupled modes of the device can be discriminated efficiently, using the harmonic admittance computation. In that case, eigenmode and harmonic admittance computations are both useful since the dispersion curves of Fig. 3 allow one to distinguish between modes that are very close to one another and not easily independently identifiable by the use of the harmonic admittance.

C. 1-3 connectivity piezocomposite

The last illustration of the proposed theory is a 1-3 connectivity piezoelectric composite. The elementary cell of the studied structure is shown in Fig. 1. The thickness was set to 300 μm, and both periodicities along x_1 and x_2 are equal to 200 μm (PZT width is 100 μm along x_1 and x_2). The same kind of analysis as for the 2-2 piezocomposite was performed. However, due to the large computation time required, the number of spatial harmonics was restricted to five for both directions, i.e., 25 terms in the series. This is a major

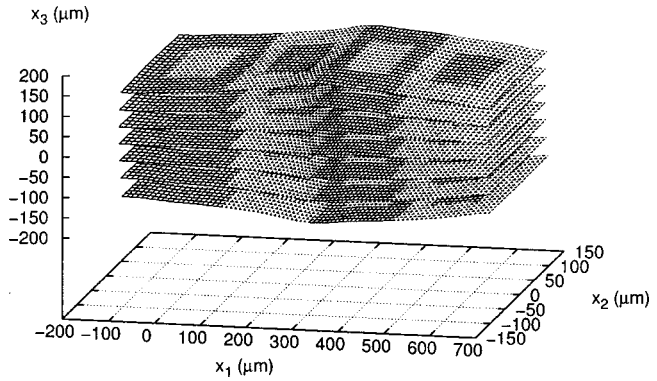

FIG. 6. First symmetrical Lamb wave propagating in four cells ($\gamma_1=0.25$, $\gamma_2=0$, $\omega=2350$ kHz) of the 1-3 piezoelectric composite of Fig. 1.

drawback of the method because computations with too small a number of harmonics yield inaccurate predictions.

Although some minima of the determinant are not physical solutions of the problem, dispersion curves for relatively low-frequency modes are found similar to those computed with a finite element method in Ref. 15.

A qualitative comparison between finite element analysis and PWE analysis of the composite is reported in Fig. 5. Although similar results are obtained in the vicinity of the longitudinal compression mode using the two methods, discrepancies arise for higher-order frequency modes. However, both approaches exhibit prohibitive computation times for the accurate simulation of high-order modes and overtones (increasing the number of elements of the finite element mesh is equivalent to increasing the number of harmonics in the PWE method).

Although the problem of accuracy must be addressed to provide reliable computation results, much pertinent information can be deduced from the proposed calculation. The shape of the mode is accessible by simply calculating the effective values of the mechanical displacement fields of the

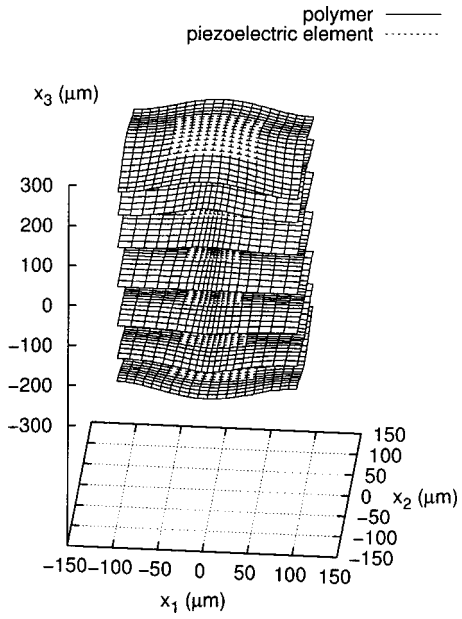

FIG. 7. Fundamental longitudinal mode along x_3 ($\gamma_1=\gamma_2=0$, $\omega=4900$ kHz) of the 1-3 piezoelectric composite of Fig. 1.

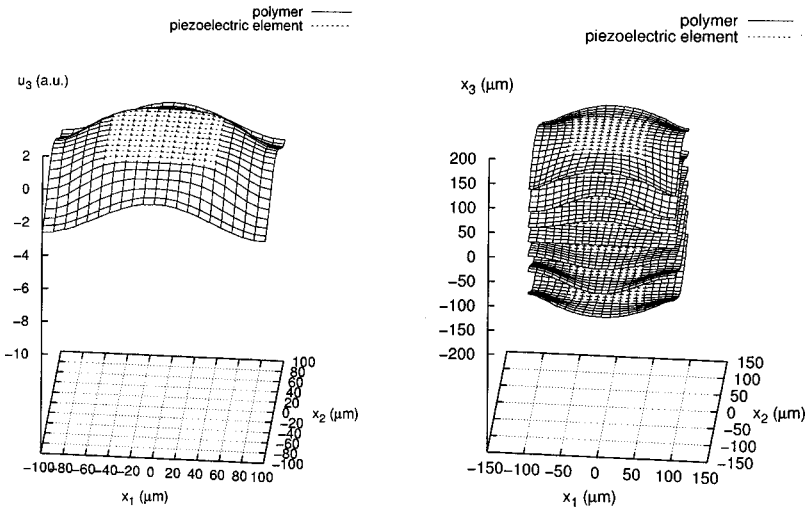

FIG. 8. First lateral mode for infinite thickness and finite thickness ($\gamma_1=\gamma_2=0$, $\omega=7200$ kHz) of the 1-3 piezoelectric composite of Fig. 1.

problem. For a given value of $(\gamma_1,\gamma_2,\omega)$, one can construct the propagation profile for the desired number of cells. This is illustrated in Fig. 6, showing the first Lamb mode at ($\gamma_1=0.25$, $\gamma_2=0$, $\omega=2350$ kHz) propagating in four adjacent cells. The mechanical state of the elementary cell for the fundamental longitudinal compression mode along x_3 and for the first lateral mode ($\gamma_1=\gamma_2=0$) are also reported in Figs. 7 and 8, respectively, demonstrating the capability of the model to fairly predict the actual vibration of a 1-3 connectivity piezoelectric composite.

Figure 9 displays the real part of the harmonic admittance (i.e., the conductance) in the first Brillouin zone[16] of the studied in-plane symmetrical structure. We can recognize for $\gamma_2=0$ the harmonic admittance of Fig. 5. Resonance frequencies are given by the maxima of the conductance. Thanks to these conductance curves, which give the resonant piezoelectrically coupled modes, and the dispersion curves calculated in the case of shorted surfaces, we are able to identify parasitic modes of the thickness mode and acoustic band-gaps of the structure, which are of main interest for ultrasonic imaging applications.

Finally, a quantitative study was performed in the case of the fundamental thickness mode. First, the longitudinal phase velocity v_l and the electromechanical coupling factor k were calculated by varying the volume fraction of ceramic, with our constant sets, according to the well-known Smith and Auld theory.[2] Then the harmonic admittance was calculated at ($\gamma_1=\gamma_2=0$) around the thickness-mode for different numbers of terms in the Bloch–Floquet and Fourier expansions. The maximum of the conductance gives one the resonance frequency f_r, while the antiresonance frequency f_a is given by the maximum of the resistance (real part of the impedance).[17] Consequently v_l and k can be calculated as follows:

$$v_l=2hf_a, \tag{36}$$

where h is the thickness of the plate, and

$$k^2=\frac{\pi}{2}\frac{f_r}{f_a}\tan\frac{\pi}{2}\frac{f_a-f_r}{f_a}. \tag{37}$$

Comparisons between theory[2] and our computations are shown in Figs. 10 and 11. By increasing the number of terms of the expansions, a convergence appears between the Smith and Auld model and the plane-wave-expansion method. For instance, with seven terms along each direction, we have a good agreement for a ceramic volume fraction from 0% to 50%.

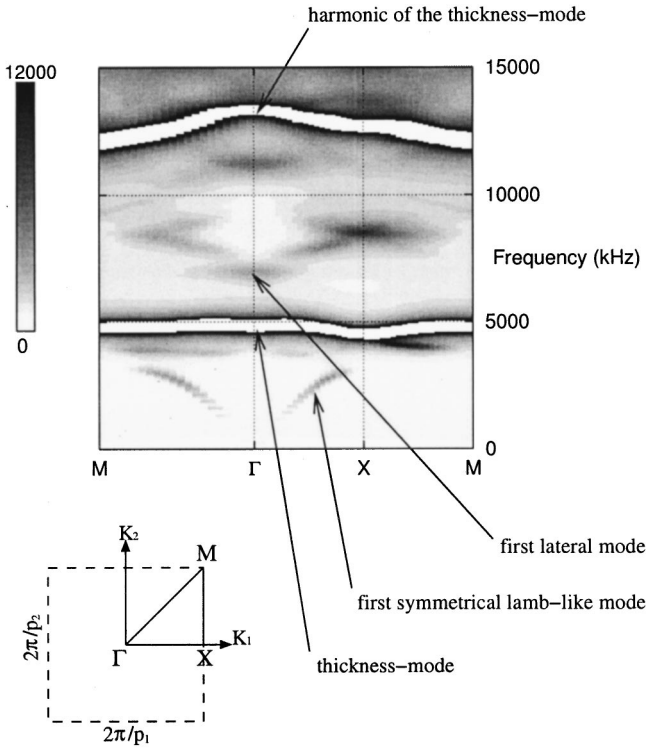

FIG. 9. Real part of the harmonic admittance, for the 1-3 piezoelectric composite, calculated in the first Brillouin zone in the (K_1,K_2) plane. One can deduce the frequencies of the parasitic modes, considering the thickness mode as the useful vibration for imaging applications. For instance, considering the path $X-M$, we can see that a vibrating mode mingles with the strong coupled fundamental thickness mode near the point X. Acoustic band-gaps are retrievable considering piezoelectrically coupled modes. The thickness mode and its harmonic are truncated (white color) because of their magnitudes.

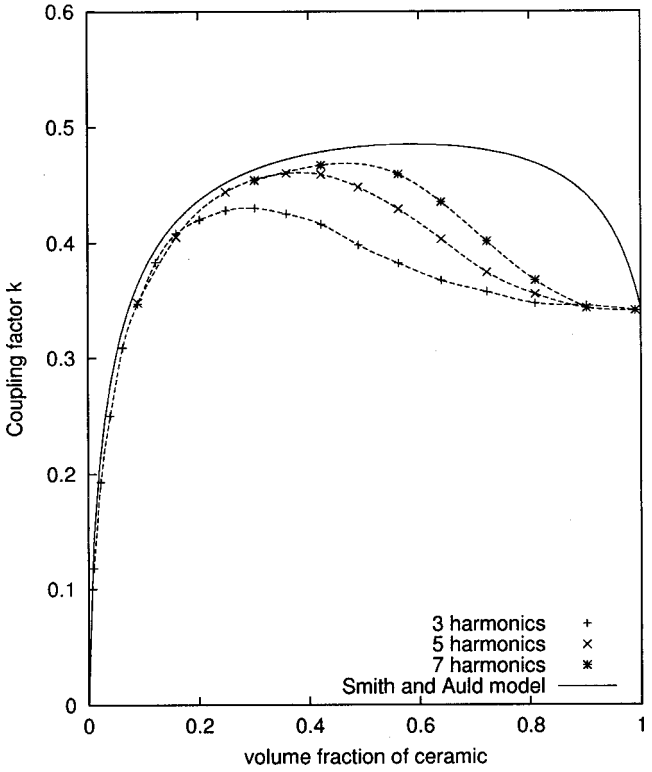

FIG. 10. Electromechanical coupling factor for the thickness mode, calculated for different values of the number of terms of the series, to be compared with the well-established Smith and Auld model. The number of harmonics along each direction is given for each computation.

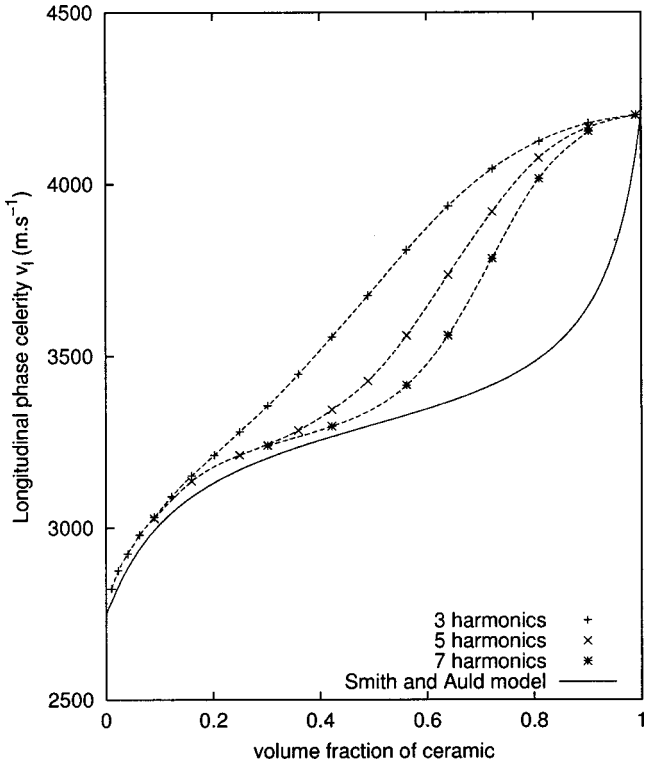

FIG. 11. Longitudinal phase velocity for the thickness mode, calculated for different values of the number of terms of the series, to be compared with the well-established Smith and Auld model. The number of harmonics along each direction is given for each computation.

IV. CONCLUSION

A full 3D model based on a plane wave expansion of the generalized acoustic fields has been developed and implemented for general piezoelectric-based composite materials. It is able to simulate homogeneous materials, but also 1D or 2D periodic devices with a good level of accuracy. It can take into account material losses using the imaginary part of elastic, piezoelectric, and dielectric fundamental constants. This approach is an alternative to finite element computations in the case of the considered regular piezoelectric composite geometry. The model is able to provide much information about the considered device such as the piezoelectric coupling, the resonance efficiency, and the effect of acoustic losses by calculating the harmonic admittance. It can incorporate different boundary conditions corresponding to effective operation of the device. First qualitative computations were performed for 2-2 and 1-3 connectivity piezoelectric composites. Complementary quantitative calculations were performed for the 1-3 connectivity piezoelectric composite thickness mode and compared to a well-established theory. In a future extension of the theory, a particular effort will be paid to the optimization of the computation time and the accuracy of 3D computations. The case of radiation in fluids and solids will also be addressed, to provide a comprehensive description of operating conditions of 2-2 and 1-3 piezoelectric composite-based devices. Even if the computation time, which governs in fact the accuracy of the method, has to be optimized, the PWE method already provides qualitative information, which is of primary interest to understand the operation of such composite structures.

ACKNOWLEDGMENTS

This work was jointly supported by the CNRS, THALES MICROSONICS (TMX), and FRAMATOME-ANP. The authors would like to thank Dr. Abdelkrim Khelif for fruitful discussions concerning the fundamentals of plane-wave-expansion methods, and also W. Steichen (TMX) and G. Pierre (FRAMATOME-ANP) for encouraging and supporting the study.

[1] B. A. Auld, *Acoustic Fields and Waves in Solids*, 2nd ed. (Krieger, Melbourne, FL, 1990).
[2] W. A. Smith and B. A. Auld, "Modeling 1-3 composite piezoelectrics: Thickness-mode oscillations," IEEE Trans. Ultrason. Ferroelectr. Freq. Control **38**(1), 40–47 (1991).
[3] R. E. Newnham, D. P. Skinner, and L. E. Cross, "Connectivity and piezoelectric-pyroelectric composites," Mater. Res. Bull. **13**, 525–536 (1978).
[4] D. Certon, F. Patat, F. Levassort, G. Feuillard, and B. Karlsson, "Lateral resonances in 1-3 piezoelectric periodic composite: Modeling and experimental results," J. Acoust. Soc. Am. **101**, 2043–2051 (1997).
[5] J. O. Vasseur, B. Djafari-Rouhani, L. Dobrzynski, M. S. Kushwaha, and P. Halevi, "Complete acoustic band gaps in periodic fibre reinforced composite materials: The carbon/epoxy composite and some metallic systems," J. Phys.: Condens. Matter **6**, 8759–8770 (1994).
[6] Y. Tanaka and S.-I. Tamura, "Acoustic stop bands of surface and bulk modes in two-dimensional phononic lattices consisting of aluminum and a polymer," Phys. Rev. B **60**, 13294–13297 (1999).
[7] A. H. Fahmy and E. L. Adler, "Propagation of surface acoustic waves in multilayers: A matrix description," Appl. Phys. Lett. **22**, 495–497 (1973).
[8] L. Boyer, "Etude Des Phénomènes de Réflexion-Réfraction Des Ondes Planes Acoustiques Dans Les Milieux Piézoélectriques," Ph.D. thesis, Université Paris 7, France, 1994.

[9] R. Courant and D. Hilbert, *Methods of Mathematical Physics* (Interscience, New York, 1953).
[10] R. C. Peach, ''A general green function analysis for SAW devices,'' in *IEEE Ultrasonics Symposium*, 1995, pp. 221–225.
[11] X. Geng and Q. M. Zhang, ''Evaluation of piezocomposites for ultrasonic transducer applications—influence of the unit cell dimensions and the properties of constituents on the performance of 2-2 piezocomposites,'' IEEE Trans. Ultrason. Ferroelectr. Freq. Control **44**(4), 857–872 (1997).
[12] Y. Zhang, J. Desbois, and L. Boyer, ''Characteristic parameters of surface acoustic waves in a periodic metal grating on a piezoelectric substrate,'' IEEE Trans. Ultrason. Ferroelectr. Freq. Control **40**(3), 183–192 (1993).
[13] R. Holland, ''Representation of dielectric, elastic, and piezoelectric losses by complex coefficients,'' IEEE Trans. Sonics Ultrason. **14**(1), 18–20 (1967).
[14] Th. Pastureaud, V. Laude, A. Soufyane, and S. Ballandras, ''Stabilization of the simulation of SAW devices on stratified structures: Application to transverse plate mode resonators,'' IEEE Int. Freq. Control Symp., 661–665 (Seattle, 2001).
[15] P. Langlet, ''Analyse de la Propagation Des Ondes Acoustiques Dans Les Matériaux Périodiques À L'aide de la Méthode Des Éléments Finis,'' Ph.D. thesis, Université de Valenciennes et du Hainaut-Cambresis, France, 1993.
[16] L. Brillouin, *Propagation in Periodic Structures* (Dover, New York, 1953).
[17] ''ANSI/IEEE standard on piezoelectricity, std 176-1987,'' IEEE Trans. Ultrason. Ferroelectr. Freq. Control **43**(5), 717–772 (1996).